Journal of
Materials Chemistry A
Materials for energy and sustainability

Accepted Manuscript

This article can be cited before page numbers have been issued, to do this please use: J. Huang, Y. Xia, S. Xu, L. Li, H. Ji, X. Chen and J. Xu, *J. Mater. Chem. A*, 2026, DOI: 10.1039/D5TA09005A.

Volume 6
Number 12
28 March 2018
Pages 4883-5230

Journal of
Materials Chemistry A
Materials for energy and sustainability
rsc.li/materials-a

ISSN 2050-7488

ROYAL SOCIETY
OF CHEMISTRY

COMMUNICATION
Zhenhai Wen *et al.*
An electrochemically neutralized energy-assisted low-cost acid-alkaline electrolyzer for energy-saving electrolysis hydrogen generation

ROYAL SOCIETY
OF CHEMISTRY

rsc.li/materials-a

View Article Online
DOI: 10.1039/D5TA09005A

# Predictive Thermal Safety of Lithium-Ion Batteries through a Unified Kinetic-Thermal Framework

Jiale Huang[1], Yiyang Xia[1], Shijia Xu[1], Ling Li[1], Hongbo Ji[1], Xiaoping Chen[1]*, Jun Xu[2, 3]*

[1]*Zhejiang Provincial International Joint Laboratory of New Energy Vehicle Technology, College of Mechanical and Automotive Engineering, Ningbo University of Technology, Ningbo, China*

[2]*Department of Mechanical Engineering, University of Delaware, Newark, DE 19716, USA*

[3] *Energy Mechanics and Sustainability Laboratory (EMSLab), University of Delaware, Newark, DE 19716, USA*

---

* Correspondence to: Dr. Jun Xu: junxu@udel.edu, Dr. Xiaoping Chen: cxp@nbut.edu.cn,

View Article Online
DOI: 10.1039/D5TA09005A

**Abstract:** Thermal runaway remains a critical barrier to the safe deployment of high-energy lithium-ion batteries. Here, we establish a unified quantitative framework that integrates intrinsic reaction kinetics with thermal transport to predict and design cell-level thermal safety. Accelerating rate calorimetry measurements are employed to resolve temperature-dependent self-heating behaviors across state of charge, providing direct inputs for a physics-based thermal model that captures both internal conduction and boundary convection. Systematic variation of state of charge, surface-to-volume ratio, and convective intensity reveals a distinct critical temperature separating stable and runaway regimes, enabling construction of a comprehensive thermal safety boundary. We show that the surface-to-volume ratio, rather than aspect ratio, serves as the fundamental geometric parameter governing temperature uniformity and heat dissipation. A dimensionless thermal safety criterion is further derived, explicitly linking self-heating to dissipation and allowing direct estimation of safe operating limits without reliance on full CFD simulations. This framework transforms thermal safety evaluation from empirical observation to a predictive, physics-informed design methodology, bridging mechanistic understanding and engineering practice to guide safe operation and scalable thermal management of lithium-ion batteries across chemistries, geometries, and cooling configurations.

**Keywords:** Thermal safety boundary; Kinetic-thermal framework; Modeling; Thermal runaway; Lithium-ion battery

View Article Online
DOI: 10.1039/D5TA09005A

## 1. Introduction

Lithium-ion batteries (LIBs) underpin the rapid expansion of electric vehicles and stationary energy storage systems, placing them at the heart of the global energy transition. However, their susceptibility to safety issues, particularly thermal runaway (TR), a self-accelerating failure process that can culminate in fire or explosion, remains a critical barrier to large-scale deployment [1-2].

Thermal runaway arises from a cascade of highly exothermic reactions that destabilize the electrochemical system once internal heat generation surpasses heat dissipation [3]. Significant progress has been made in characterizing these reactions at the materials level (e.g., solid–electrolyte interphase decomposition, electrolyte oxidation, cathode oxygen release) [4-10] and the component level (e.g., electrode–electrolyte interfaces, current collectors, separators) [11-16]. Advanced diagnostic tools such as accelerating rate calorimetry (ARC) [17-20], differential scanning calorimetry (DSC) [21-22], and *in situ* imaging and gas analysis [23-25] have revealed the temporal sequence, onset temperatures, and energetics of these reactions. Complementary propagation studies have further elucidated how localized instabilities evolve into full-cell runaway by coupling reaction kinetics, heat generation, and thermal transport [26-29]. Collectively, these investigations have established a detailed mechanistic understanding of TR initiation and evolution.

At the cell scale, however, thermal runaway is governed not only by chemical reactivity but by the dynamic competition between internal heat generation and external heat dissipation. This balance is strongly influenced by state of charge (SOC) [30], intrinsic thermal conductivity

View Article Online
DOI: 10.1039/D5TA09005A

and anisotropy [31], and boundary cooling conditions [32]. When self-heating exceeds heat dissipation, nonlinear positive feedback leads to rapid temperature escalation. Although prior studies have proposed critical temperatures or heat generation thresholds [33-36], such criteria are typically geometry- or condition-specific. For instance, while geometric metrics like the aspect ratio are often used to characterize cell shape, they primarily describe the internal heat conduction distance. They fail to capture the fundamental competition between volumetric heat generation and surficial heat dissipation. Recently, data-driven approaches, particularly machine learning, have emerged as promising tools for predicting thermal runaway risks by learning complex nonlinear patterns from large datasets [37]. In this light, combing data-driven insights with physics-based transport laws offers a robust pathway for safety prediction. Consequently, a unified, quantitative, and physically grounded thermal safety criterion that incorporates capacity, geometry, and environmental factors remains elusive.

To address this gap, we develop a comprehensive framework that explicitly couples intrinsic heat generation with external heat dissipation to construct a mechanistic thermal safety boundary for cylindrical LIBs. First, intrinsic self-heating behavior across SOCs is experimentally quantified using ARC under adiabatic conditions, providing temperature-dependent heat generation profiles. These data are integrated into a three-dimensional thermal model that resolves internal conduction and boundary convection under varying cooling intensities. By systematically varying SOC, surface-to-volume ratio, and convective heat transfer coefficient, we identify the critical temperature separating stable and runaway regimes. To generalize these discrete results, a random forest model is trained to construct a continuous, predictive thermal safety boundary.

View Article Online
DOI: 10.1039/D5TA09005A

Finally, inspired by Semenov's thermal explosion theory, we derive a dimensionless thermal safety criterion (TSC) that quantitatively balances self-heating and dissipation, enabling rapid estimation of safe operating limits without full computational fluid dynamics (CFD) simulations.

Unlike case-specific thresholds or purely empirical approaches, this unified kinetic–thermal framework is physics-informed, scalable, and directly applicable to design. By integrating experimental calorimetry, numerical modeling, machine learning, and theoretical analysis, this work transforms thermal safety evaluation from empirical observation into a predictive, design-oriented methodology for assessing and optimizing the thermal stability of lithium-ion batteries across chemistries, geometries, and cooling strategies.

## 2. Thermodynamics of thermal runaway

### 2.1 Thermal runaway characteristics

The TR behavior of a commercial 18650 NCM cylindrical cell was evaluated using ARC under adiabatic self-heating conditions representative of worst-case failure scenarios. Prior to testing, the cell's physical properties and cycling consistency were verified to ensure data reliability (Figure S1).

Despite differences in stored energy, all cells follow four characteristic stages: (1) heat-wait-seek, (2) self-heating, (3) venting, and (4) runaway. However, the onset temperature of self-heating is strongly SOC-dependent (Figure 1 (a)). At 100% SOC, self-heating begins near 48 ℃, whereas at 0% and 50% SOC it is delayed until 100 ℃, reflecting the increased reactivity of high-energy cathode, electrolyte, and anode interfaces at elevated SOCs. In the meantime, the transition temperature to runaway decreases with increasing SOC, reflecting that enhanced reactivity has a

View Article Online
DOI: 10.1039/D5TA09005A

consistent trend that aligns with the four stages. The peak temperature during runaway exceeds 370 ℃. It is noted that the recorded maximum temperatures across different SOCs are similar. However, this is attributed to the mechanical detachment of the thermocouples caused by violent gas release and combustion, which prevents the capture of the true maximum temperature. Nevertheless, the kinetic parameters derived from the earlier self-heating phase remain continuous and reliable, providing sufficient input for the thermal safety model.

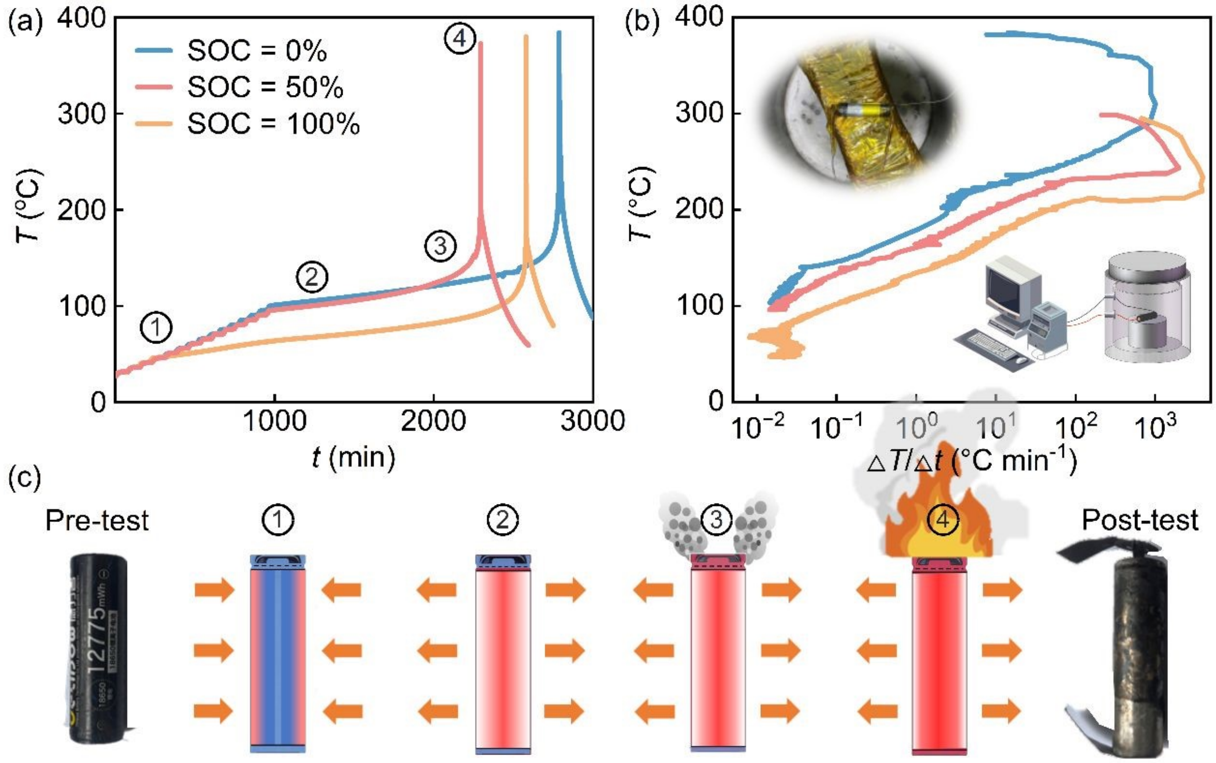

**Figure 1.** Thermal runaway characterization of a commercial 18650 NCM cell using ARC.
(a) Temporal evolution of cell temperature at different states of charge (SOC = 0%, 50%, and 100%) under adiabatic conditions, revealing four characteristic stages: (1) heat–wait–seek, (2) self-heating, (3) venting, and (4) runaway. The onset of self-heating shifts to lower temperatures with increasing SOC, while the runaway transition consistently occurs near 150 °C.
(b) Corresponding temperature rise rate ($\Delta T/\Delta t$) profiles showing the exponential escalation of self-heating as the system transitions from controlled heating to thermally unstable regimes. Insets illustrate the experimental setup and post-run deformation of the cell.
(c) Schematic depiction of the TR sequence and associated energy redistribution processes, from

View Article Online
DOI: 10.1039/D5TA09005A

pre-test to post-run conditions. The sequence highlights the transition from external heating to internally driven reaction-dominated runaway, consistent with observed structural failure and ejection following combustion.

The corresponding temperature rise rates (Figure 1 (b)) reveal the dynamic nature of the runaway process. Below 100 ℃, the temperature evolution is dominated by ARC's controlled heating protocol. Once self-heating initiates, the rate increases exponentially with temperature, reflecting the kinetic acceleration of exothermic reactions. At comparable temperatures, higher SOCs exhibit markedly steeper rise rates, confirming that cells sorting more energy not only generate more heat but also accelerate feedback-driven instability.

Prior to self-heating, heat is externally supplied and partially dissipated through the cell surface (Figure 1 (c)). Once self-heating begins, external heating is disabled and the system transitions to a quasi-adiabatic state, where temperature evolution is governed almost entirely by internal reaction kinetics. Pre- and post-test photographs further confirm severe deformation and rupture, consistent with rapid internal pressure buildup during the runaway event (Figure 1 (c)). The measured temperature rise rate was then converted into the heat generation rate using

$$Q_{\mathrm{gen}} = mc_{\mathrm{p}}\frac{\Delta T}{\Delta t} \tag{1}$$

where $m$ is the cell mass and $c_{\mathrm{p}}$ is the specific heat capacity (measured in Supplementary Section 1). This transformation enables direct quantification of intrinsic reaction power as a function of temperature. To capture the nonlinear thermal behaviors, the heat generation profiles were fitted using a piecewise function, linear in the low-temperature regime and exponential beyond the onset of self-heating. These temperature-dependent expressions were subsequently used as physically grounded heat source term in the numerical simulations. It is acknowledged that this formulation

View Article Online
DOI: 10.1039/D5TA09005A

correlates heat generation solely with temperature, effectively treating the reaction kinetics as zero-order with respect to reactant concentration. While this simplifies the complex multi-step depletion mechanisms, it provides a conservative upper bound for heat generation. For the specific purpose of identifying the critical safety boundary, this approach ensures that the predicted safe operating limits are robust, as they do not rely on reactant consumption to aid stabilization.

### 2.2 Determination of critical temperature

A numerical simulation framework was developed to resolve the coupled thermal processes governing the transition between stabilization and runaway. The model captures internal conduction and surface convection under externally imposed initial temperature conditions. Throughout the simulations, the ambient temperature $T_{\mathrm{amb}}$ was fixed at 25 ℃, while the initial cell temperature $T_0$ was systematically varied to determine the stability threshold. It is also worth noting that the simulations are initialized with a uniform temperature field, whereas real-world abuse scenarios often involve thermal gradients. This uniform initialization serves as a conservative design assumption. The thermal properties of the cell, anisotropic thermal conductivity (Figures S2 and S3) and specific heat capacity (Figure S4) have been carefully measured. The grid and time-step independence have been verified (Figure S5). To determine the threshold for thermal failure, the initial cell temperature was systematically varied in 1 ℃ increments. For each numerical simulation, a virtual probe recorded the peak temperature in the domain, enabling classification of the final state as either chill down or runaway.

For a 100% SOC 18650 cell subjected to convective coefficients of 1, 5, and 20 $\mathrm{W \cdot m^{-2} \cdot K^{-1}}$, representative initial temperature windows of 126-131 ℃, 151-156 ℃, and 168-173 ℃ were

View Article Online
DOI: 10.1039/D5TA09005A

examined, respectively (Figures 2 (a)-(c)). Two distinct regimes emerged. In the *runway* regime, internal thermal feedback dominated, and the temperature diverged rapidly. In the *chill-down* regime, the cell cooled back to equilibrium as heat removal dominated over self-heating. Additionally, Figures 2 (d)-(f) present the temporal evolution of the maximum temperature for three representative cases: prior to runaway initiation, at the onset of thermal runaway, and during the stabilization phase of chill-down. The critical temperature $T_c$ was thus defined as the highest initial condition that still results in stabilization, providing a quantitative boundary between safe and unsafe thermal trajectories.

To clarify the underlying physics, three representative states were extracted from the simulations (Figures 2 (g)-(i)). In the pre-runaway stage ($h = 1$ W·m$^{-2}$·K$^{-1}$, $T_0 = 130$ °C), internal temperature ranged only from 160 °C to 172 °C, indicating efficient heat redistribution through conduction and moderate surface losses. Once the runaway was triggered, the peak temperature surged to 250 °C within seconds, and a pronounced spatial gradient emerged, signifying strong positive feedback and loss of thermal equilibrium. In contrast, under high convection ($h = 20$ W·m$^{-2}$·K$^{-1}$, $T_0 = 168$ °C), the system remained thermally stable and nearly isothermal, with $< 0.2$ °C variation across the domain.

These results clearly demonstrate that the transition between stabilization and runaway is governed by the interplay between intrinsic reaction kinetics and external heat removal capacity. The identified $T_c$ thus serves as a mechanistic indicator of the boundary separating self-limiting and self-accelerating thermal responses in lithium-ion cells.

View Article Online
DOI: 10.1039/D5TA09005A

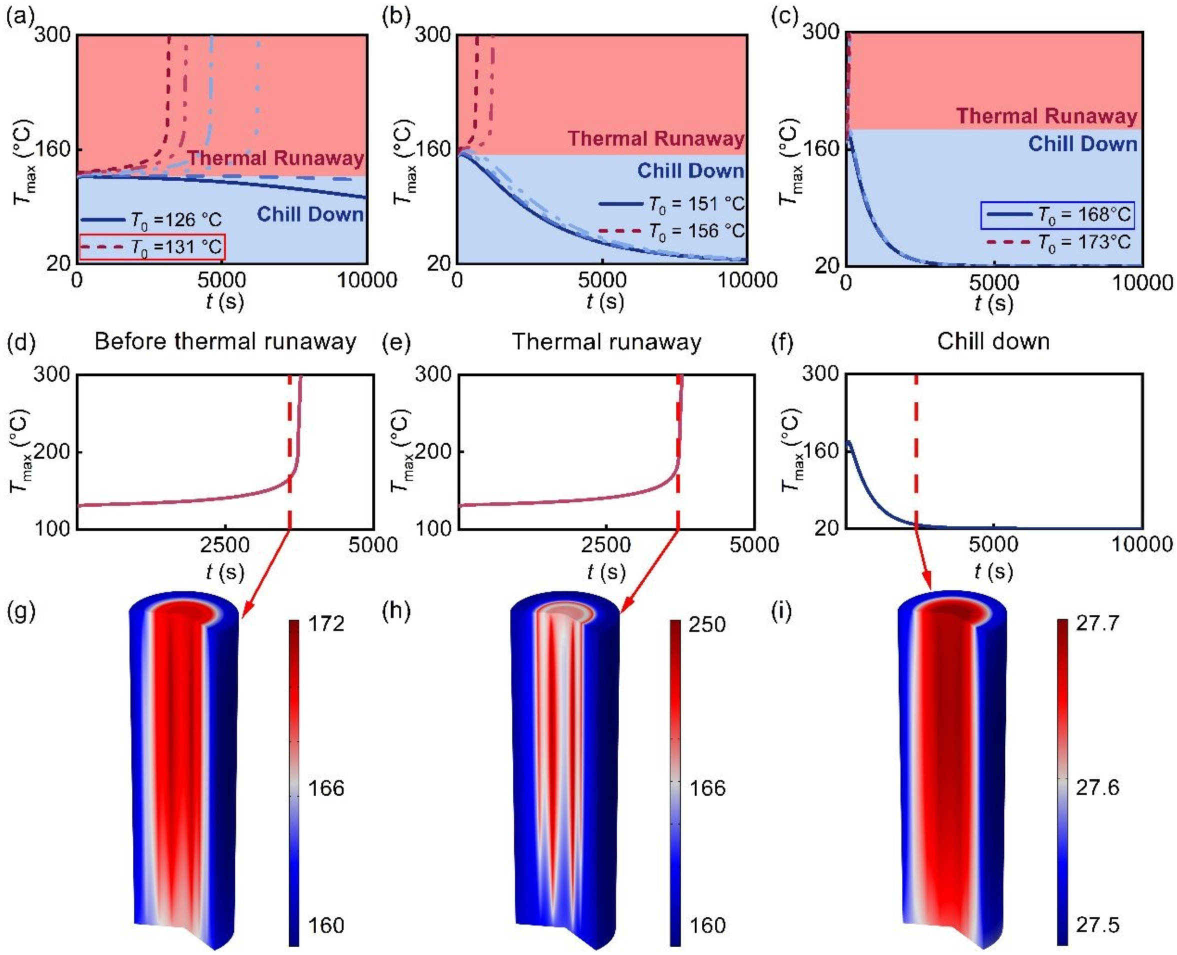

**Figure 2.** Numerical determination of the critical temperature separating thermal runaway from stabilization in a cylindrical 18650 NCM cell.

(a)–(c) Simulated temperature evolution showing the transition between thermal runaway and chill-down regimes at convective heat transfer coefficients of (a) 1, (b) 5, and (c) 20 W·m⁻²·K⁻¹. Each case compares two representative initial temperatures ($T_0$), with the red-shaded region indicating runaway and the blue-shaded region indicating stabilization.

(d)–(f) Temporal evolution of peak temperature ($T_{\max}$) for three representative cases: (d) before triggering, (e) at the onset of thermal runaway, and (f) during chill-down stabilization.

(g)-(i) Temperature contour snapshots for three representative cases: (g) before triggering, (e) at the onset of thermal runaway, and (f) during chill-down stabilization.

## 3 Interplay of heat dissipation and geometry in thermal stability

Beyond SOC, thermal stability in lithium-ion cells is strongly governed by two system-level factors: the external thermal environment and the cell geometry. The former dictates the rate of heat removal through surface convection, while the latter influences both internal temperature

View Article Online
DOI: 10.1039/D5TA09005A

uniformity and the efficiency of boundary-mediated dissipation.

During external heating, the front develops in an irregular, nonuniform pattern due to the nonlinear temperature dependences of reaction kinetics (Figures 3 (a) and (b)). In contrast, during cooling, the front becomes elliptical, shaped by the near-linear decay of temperature and the intrinsic anisotropy of thermal conductivity within the jelly-roll structure. This directional dependence underscores that thermal runaway onset is not purely kinetically controlled but also governed by spatial heat transport. Increasing the external heat transfer coefficient shifts the system toward greater stability, raising the threshold for runway (Figure 3 (c)). However, beyond approximately 20 $W \cdot m^{-2} \cdot K^{-1}$, further increases yield diminishing returns, marking a practical upper limit for forced-air cooling in realistic designs. Beyond this threshold, geometric or material-level optimization is required to achieve additional safety margins.

While the aspect ratio has been widely used to describe geometric effects in prior studies, impacting heat spreading [38], propagation velocity [39], and convective performance [40-43], it treats geometry primarily as a shape descriptor and does not explicitly couple internal transport with external removal. This raises the question of whether the aspect ratio can serve as a universal indicator when heat release and thermal extraction act simultaneously. The surface-to-volume ratio ($S/V$) provides a more physically grounded metric, as it directly represents the balance between heat accumulation and the surface-mediated dissipation. Its relevance has been demonstrated in systems ranging from biological heat regulation to ionic transport in electrochemical cells [44-46]. It is acknowledged that due to the anisotropic thermal conductivity of LIBs, the aspect ratio influences the internal heat conduction path and temperature uniformity. However, for the

View Article Online
DOI: 10.1039/D5TA09005A

determination of the critical thermal safety boundary, the global energy balance is paramount. Since intrinsic heat generation is volumetric while dissipation is surficial, the competition between these two fluxes is mathematically governed by the surface-to-volume ratio ($S/V$). Consequently, laboratory-scale runaway studies have linked S/V to the rate of temperature escalation [47], confirming its role as the dominant geometric criterion for macro-scale safety evaluation. Theoretical modeling (Figure S6) and parametric investigations (Figure S7) further confirm that $S/V$ intrinsically governs the transient thermal response of reactive solids [48] .

To isolate the impact of geometric configuration on thermal stability, the parametric study in Figure 3 (d)-(e) was conducted under a constant total volume constraint. Consequently, the total heat generation power remained identical across all cases, ensuring that the variations in temperature distribution were driven solely by the differences in internal thermal conduction resistance and surface dissipation area, rather than variations in total thermal energy. Across all SOCs, the critical temperature increases monotonically with S/V, demonstrating that the enhanced surface accessibility improves both energy dissipation and temperature homogenization. Collectively, these results establish S/V as a unified geometric parameter that captures the coupled effects of heat redistribution and boundary interaction, enabling more accurate prediction and design of thermal safety thresholds than aspect ratio alone. It is worth noting, however, that the metric assumes the internal heat transport is sufficient to utilize the available surface area. In cell geometries with extreme aspect ratios, such as very elongated or extremely flat configurations, the significant thermal anisotropy could lead to directional heat transfer bottlenecks. In such limit cases, the preferred direction of heat flow might decouple the effective cooling area from the total

View Article Online
DOI: 10.1039/D5TA09005A

surface area, potentially complicating the single dependence on S/V. Nevertheless, for standard cylindrical form factors, S/V remains the dominant predictor of the global thermal safety boundary.

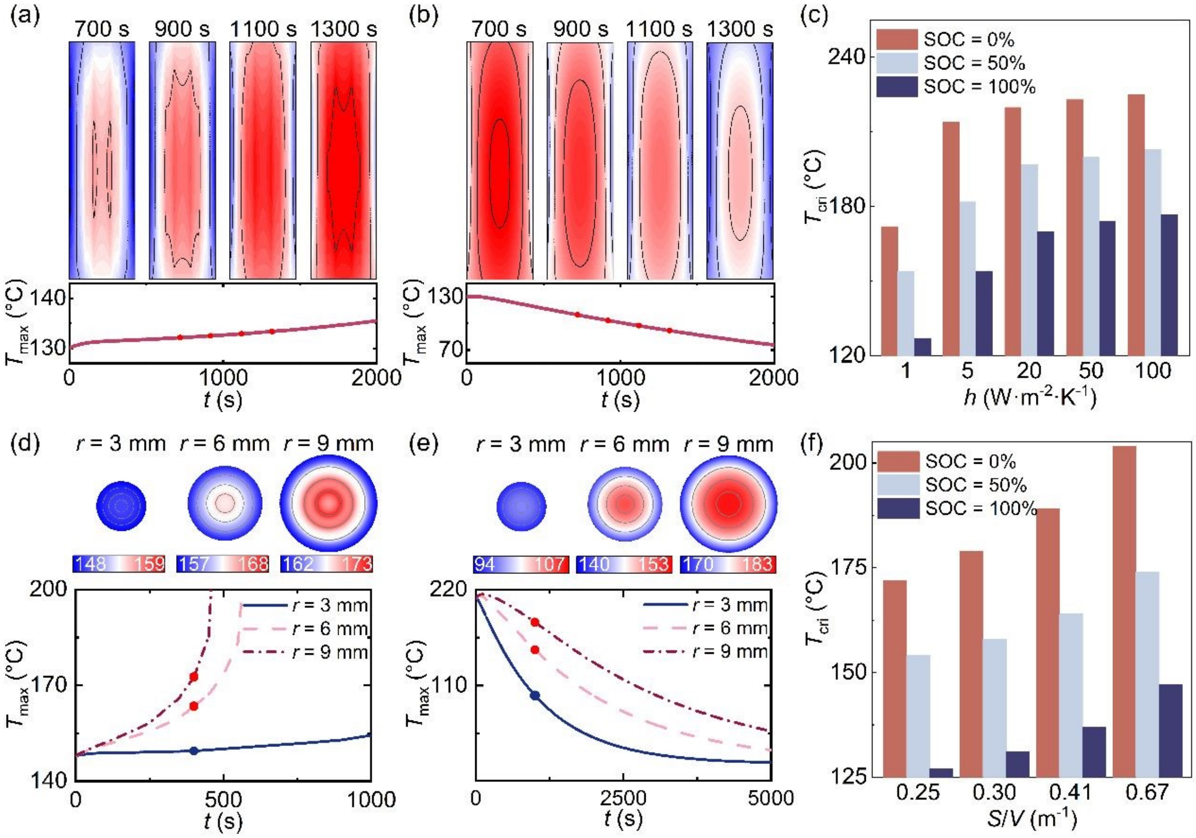

**Figure 3.** Influence of convective intensity and geometric configuration on thermal stability of cylindrical lithium-ion cells.

(a)-(b) Spatiotemporal evolution of internal temperature fields during (a) external heating and (b) subsequent cooling, showing the progression and regression of thermal fronts. The shape transition from irregular to elliptical contours reflects the nonlinear temperature dependence of reaction kinetics and anisotropic thermal conductivity in the jelly-roll structure.

(c) Variation of the critical temperature ($T_c$) with convective heat transfer coefficient (h) across different states of charge (SOCs). Enhanced convection raises the stabilization threshold, with diminishing returns beyond ≈20 W·m$^{-2}$·K$^{-1}$.

(d)-(e) Effect of cell diameter ($r$ = 3, 6, and 9 mm) on temperature evolution during (d) heating and (e) cooling. Insets show corresponding cross-sectional temperature distributions, where smaller radii (larger surface-to-volume ratio) yield more uniform internal temperatures and reduced core heating.

(f) Dependence of the critical temperature on surface-to-volume ratio ($S/V$) at a fixed convective coefficient (h = 1 W·m$^{-2}$·K$^{-1}$). Higher $S/V$ ratios improve heat dissipation and delay the onset of runaway across all SOCs, establishing $S/V$ as a unified geometric parameter governing the

View Article Online
DOI: 10.1039/D5TA09005A

coupling between heat redistribution and boundary-mediated cooling.

## 4 Predictive mapping of thermal stability regimes

### 4.1 Construction of the thermal safety boundary

Using the validated simulation dataset spanning SOC, convective intensity, and surface-to-volume ratio, we constructed a thermal safety boundary that defines the maximum initial temperature a cell can withstand without entering runaway. To generalize discrete simulation outputs into a continuous and predictive design space, a machine-learning model based on random forest regression was trained and validated (Figures S8 and S9).

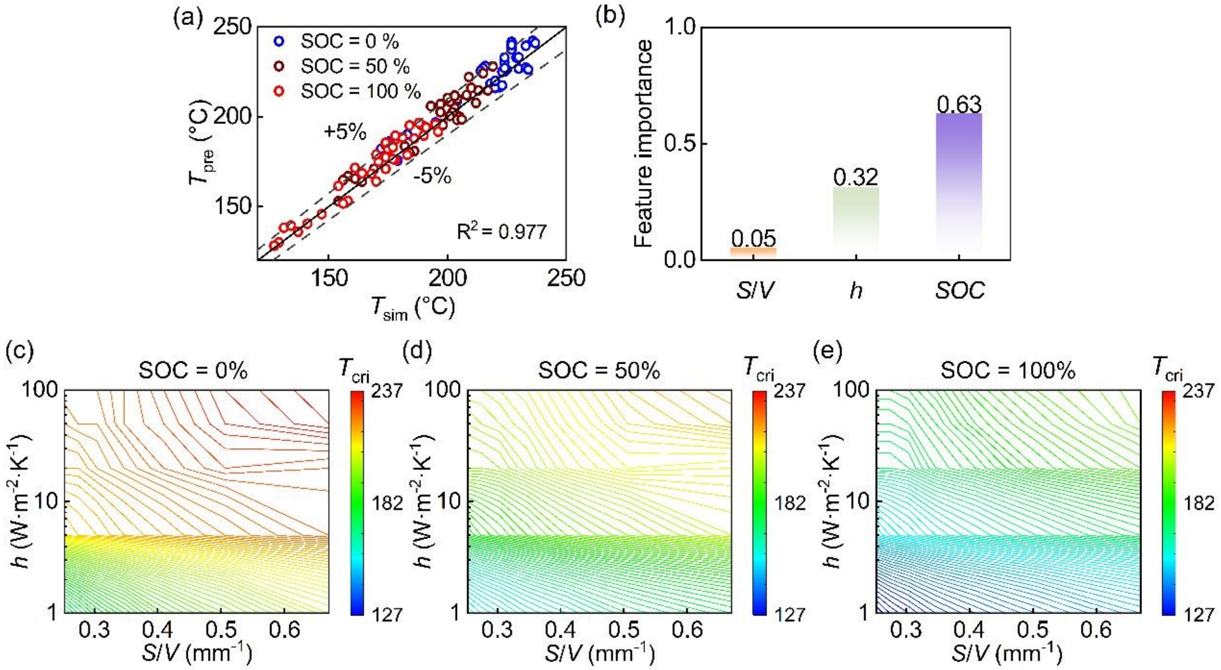

**Figure 4.** Machine learning-based temperature prediction and thermal safety boundary mapping. (a) Comparison between machine learning predictions ($T_{pre}$) and simulated temperatures ($T_{sim}$) for SOC values of 0%, 50%, and 100%. The predicted temperatures exhibit a strong linear correlation with the simulated data, showing a maximum deviation of 7.54%, with over 80% of values falling within ±5%, and $R^2 = 0.977$.

(b) Feature importance of input parameters derived from the trained model. Insets show that SOC has the greatest influence (0.63), followed by the heat transfer coefficient (h) (0.32) and the surface-to-volume ratio (*S*/*V*) (0.05).

(c)-(e) Thermal safety boundary mapping across the parameter space at SOCs of 0% (c), 50% (d),

View Article Online
DOI: 10.1039/D5TA09005A

and 100% (e). Insets illustrate that higher SOC, larger surface-to-volume ratio (*S*/*V*), and enhanced heat transfer coefficients (*h*) broaden the safety boundary, with the maximum safe temperature reaching 237 °C.

The trained machine-learning model exhibits strong agreement ($R^2 = 0.977$), with > 80% of cases within ±5% error and a maximum deviation of 7.54%, demonstrating its robustness in capturing nonlinear interactions among parameters (Figure 4 (a)). The feature importance analysis indicates that SOC is the dominant factor (weight = 0.63) (Figure 4 (b)), reflecting its control over reaction enthalpy and kinetic intensity. The convective parameter (weight = 0.32) ranks second, confirming the substantial impact of thermal management in delaying runaway onset. Although *S*/*V* contributes a smaller global weight value (0.05) due to the dominance of convective cooling at high *h* values, it remains essential in the weak convection regime typical of passive cooling or failure scenarios. Quantitative analysis of the simulation results (Figure 3(f)) reveals that at $h = 1$ $\mathrm{W\cdot m^{-2}\cdot K^{-1}}$, increasing *S*/*V* from 0.25 to 0.67 $\mathrm{m^{-1}}$ raises the critical temperature by more than 20℃ at 50% SOC. This indicates that while geometry is secondary under strong active cooling, it provides a significant safety margin improvement when external heat dissipation is limited.

In the resulting thermal safety boundary as a contour map in the multidimensional parameter space, each contour denotes a critical temperature corresponding to a specific combination of SOC, *S*/*V*, and convection level (Figures 4 (c)-(e)). This boundary provides a direct, design-oriented tool: given operating conditions and cell geometry, one can determine the maximum allowable temperature without solving the full thermal model. Conversely, it can be used inversely to identify the minimum cooling requirement or geometric constraint necessary to maintain stability. By integrating the coupled influences of material state, geometry, and environment into a single

View Article Online
DOI: 10.1039/D5TA09005A

predictive framework, the thermal safety boundary bridges mechanistic insight with engineering practicality, enabling quantitative design of cell-level safety margins.

### 4.2 Dimensionless thermal safety criterion

While the thermal safety boundary defines the safe operational envelope implicitly, practical design requires an explicit, physically interpretable stability index. To this end, we derive a dimensionless thermal safety criterion (TSC) grounded in the fundamental energy balance of a reactive system. According to Semenov's theory, thermal stability is achieved when the rate of reaction-driven heat release equals the rate of thermal loss to the surroundings [[49] ]. At the critical temperature $T_{\mathrm{cri}}$, this steady-state balance can be expressed as,

$$Q_{\mathrm{gen}}(T_{\mathrm{cri}},\ SOC) = Q_{\mathrm{diss}}(T_{\mathrm{cri}}) \tag{2}$$

Let $q_{\mathrm{gen}}$ ($T$, SOC) denote the volumetric reaction power, so that

$$Q_{\mathrm{gen}}(T,\ SOC) = Vq_{\mathrm{gen}}(T,\ SOC) \tag{3}$$

Assuming convective boundary losses, the corresponding dissipation term becomes

$$Q_{\mathrm{diss}} = hS(T - T_{\mathrm{amb}}) \tag{4}$$

Combining Eqs. (2)-(4) yields a dimensionless thermal safety criterion (TSC)

$$TSC = \frac{h\left(\frac{S}{V}\right)(T_{\mathrm{cri}} - T_{\mathrm{amb}})}{q_{\mathrm{gen}}(T_{\mathrm{cri}}, SOC)} \tag{5}$$

which quantifies the balance between dissipation potential and intrinsic reaction power at the threshold of instability. In an ideal lumped system, TSC = 1. However, real cells exhibit temperature gradients, nonuniform kinetics, and spatial heat losses, leading to deviations that must be calibrated.

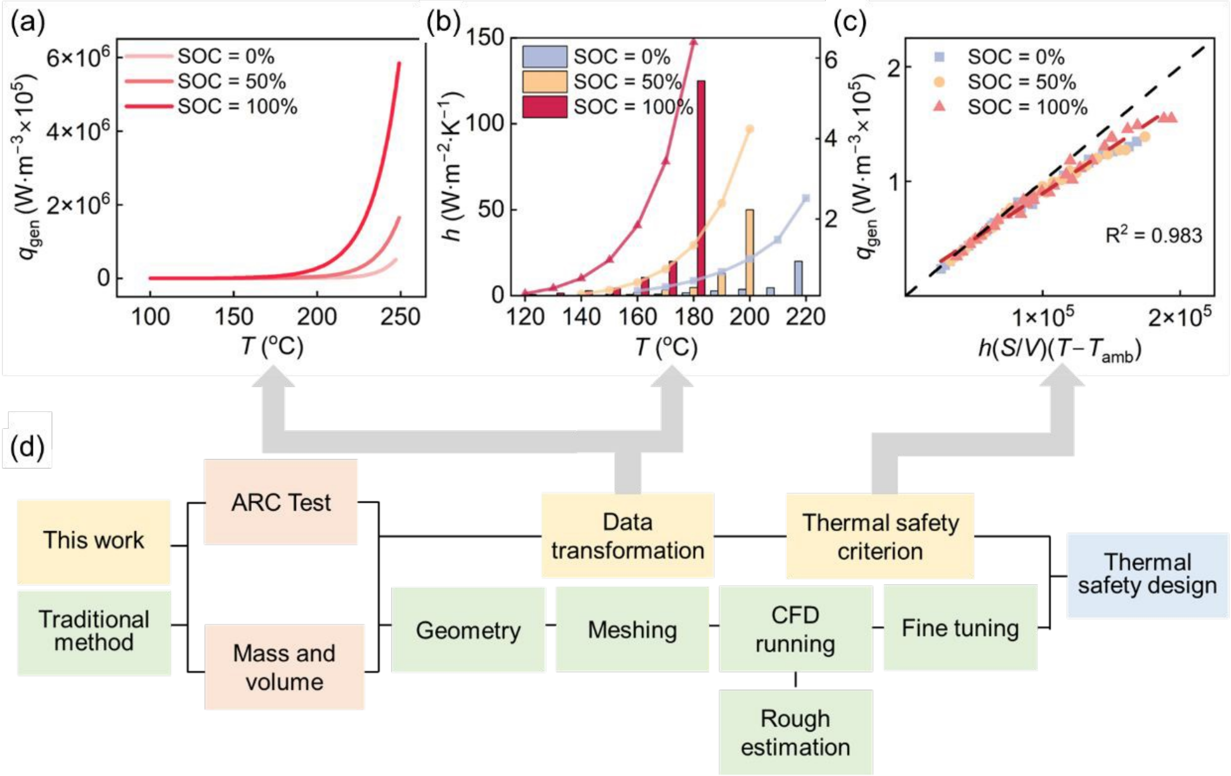

**Figure 5.** Development and application of the thermal safety criterion (TSC) and comparison of design workflows.

(a) Volumetric heat generation rate ($q_{gen}$) as a function of temperature, showing an exponential rise at elevated temperatures. Insets highlight that $q_{gen}$ increases by orders of magnitude with higher SOC prior to runaway initiation.

(b) Thermal safety boundary illustrating the relationship between convective intensity and volumetric heat generation at each temperature. For a given temperature, the required heat transfer coefficient ($h$) scales approximately with $q_{gen}$, reflecting the balance between internal thermal stress and external cooling capacity.

(c) Linear regression used to formulate the thermal safety criterion. The strong linear correlation between $q_{gen}$ and $h(S/V)(T - T_{amb})$ (R² = 0.983) confirms their proportionality, while the slight slope deviation from the diagonal reflects the influence of temperature gradients and non-lumped behavior.

(d) Comparison between the conventional thermal safety design workflow and the streamlined approach enabled by the TSC. The proposed method eliminates geometry reconstruction, mesh generation, and iterative CFD simulations, replacing them with direct data transformation using the TSC, thereby enabling rapid and scalable thermal safety design.

To incorporate realistic effects, we refine the criterion using the previously constructed thermal safety boundary. The ARC-derived $q_{gen}$ (Figure 5(a)) shows a clear dependency on SOC and increases exponentially above 200 °C. As the heat generation rate rises, greater convective

View Article Online
DOI: 10.1039/D5TA09005A

cooling is required for stabilization, highlighting the proportional relationship between dissipation and heat generation (Figure 5(b)). This aligns with the proportionality implied by Eq. (5), suggesting that $q_{\mathrm{gen}}$ and $h(S/V)(T\text{-}T_{\mathrm{amb}})$ can be directly regressed. Further, the linear regression (Figure 5 (c)) ($R^2 = 0.983$) confirms the validity of the theoretical framework with minor deviations attributed to replacing surface temperature with the domain maximum in the calculation of $T\text{-}T_{\mathrm{amb}}$. This regression allows for the derivation of the thermal safety criterion, so that we obtain

$$TSC = 1.252 \tag{6}$$

which serves as an effective stability threshold within the investigated range. It is important to note that while the mathematical framework of the TSC is derived from fundamental energy conservation and is thus applicable to any battery chemistry, the specific coefficient represents a geometric correction for the cylindrical jellyroll structure. For systems with significant different thermal transport properties or geometries, this coefficient may require recalibration to account for variation in the Biot number. Crucially, the primary contribution of this work is the establishment of a systematic methodology to drive this critical threshold. By following the proposed workflow, integrating kinetic parameterization with targeted thermal simulation, this safety criterion can be determined for diverse battery chemistries and form factors.

This criterion enables a direct pathway to construct thermal safety boundaries without repeated numerical simulations (Figure 5 (d)). Traditionally, determining safe operating limits required extensive meshing, CFD execution, and iterative tuning. In contrast, once $q_{\mathrm{gen}}(T)$ is derived from ARC data, the TSC allows immediate calculation of the required product $h(S/V)$ for a target allowable temperature. Engineers can therefore invert the criterion to determine the

View Article Online
DOI: 10.1039/D5TA09005A

minimum cooling requirement or optimal geometry needed to prevent runaway.

By distilling a complex thermo-kinetic process into a concise, physics-informed stability index, the dimensionless thermal safety criterion provides a unified tool for cell design, cooling strategy optimization, and rapid safety evaluation across chemistries, geometries, and operational environments.

## 5 Conclusions

This study establishes a unified and quantitative framework for predicting and designing thermal safety in cylindrical lithium-ion cells by integrating experimentally derived self-heating behavior with numerical simulation and data-driven modeling. Using ARC to capture intrinsic reaction kinetics, we resolved the coupled interaction between internal thermal feedback and external heat removal across a wide design space of state of charge, convective environment, and geometric configuration. From these results, we constructed a thermal safety boundary, identified surface-to-volume as a physically meaningful geometric descriptor, and derived a dimensionless thermal safety criterion that directly links fundamental thermal processes to practical design constraints. Collectively, these advances provide a mechanistic, scalable, and design-oriented pathway for preventing thermal runaway in high-energy lithium-ion cells.

(1) Construction of a thermal safety boundary

Over 300 simulations were performed to identify the critical temperature that separates thermal runaway from stabilization across SOC (0-100%), convection (1-50 $W \cdot m^{-2} \cdot K^{-1}$), and geometry. A random forest model accurately predicted these outcomes ($R^2 = 0.977$, max deviation 7.54%, >80% within 5%), capturing nonlinear interactions between parameters. Feature

View Article Online
DOI: 10.1039/D5TA09005A

importance analysis showed SOC as the dominant factor (0.63), followed by convective intensity (0.32) and geometry (0.05). The boundary revealed that increasing cooling capacity shifts cells toward higher stability, but gains plateau beyond 20 W·m$^{-2}$·K$^{-1}$, establishing a practical benchmark for forced-air thermal management. The resulting map provides a direct tool for determining the maximum allowable temperature under any combination of operating and design parameters.

(2) Surface-to-volume ratio as a unifying geometric metric

We demonstrate that $S/V$ provides a more fundamental and mechanistically grounded geometric parameter than aspect ratio because it simultaneously governs internal temperature uniformity and boundary-mediated heat removal. Increasing $S/V$ from 0.25 to 0.67 m$^{-1}$ improved thermal homogeneity and raised the critical temperature by more than 20 ℃ at 50% SOC and $h$ = 1 W·m$^{-2}$·K$^{-1}$. $S/V$ also modulates the sensitivity of the system to convection. Under weak cooling ($h \leq 5$ W·m$^{-2}$·K$^{-1}$), geometry exerts a strong influence on stability, whereas under strong cooling ($h \geq 20$ W·m$^{-2}$·K$^{-1}$), geometric effects saturate. Thus, $S/V$ serves as a unified metric that captures the coupled influence of internal transport and external dissipation within the thermal safety boundary and provides a design-relevant handle for engineering thermal robustness.

(3) Thermal safety criterion for rapid and physics-informed design

Inspired by Semenov's theory, we derived a dimensionless thermal safety criterion (TSC) that identifies the condition at which thermal feedback is exactly balanced by dissipation. Regression against critical-state simulation data confirmed the linear relationship between volumetric self-heating and $h(S/V)(T-T_{\mathrm{amb}})$, yielding TSC = 1.252 with $R^2 = 0.983$. Unlike traditional workflows that rely on iterative CFD simulation, the TSC enables direct calculation of the maximum safe

View Article Online
DOI: 10.1039/D5TA09005A

operating temperature, or, inversely, the minimum required cooling or geometric configurations from ARC-derived thermal reactivity. This transforms thermal safety evaluation from trial-and-error modeling into an explicit, physics-informed formulation, offering a scalable and practical tool for battery design, parameter optimization, and safety certification.

## 6 Methodology

### 6.1. Cell specifications and preliminary characterization

A commercial 18650-type NCM cell (Delipow, 3500 mAh nominal capacity, 3.7 V nominal voltage, 4.2 V cutoff) was selected for all experiments. To ensure data reliability, a consistency test was performed on ten units using a battery cycler, verifying comparable voltage–capacity behavior over nine charge–discharge cycles (Figure S1). Fundamental physical properties, including mass, dimensions, and volume, were measured with a high-precision analytical balance (Sartorius BSA224S, 0.1 mg resolution) and a vernier caliper (Figure 6 (a)). The average mass was $4.56\times10^{-2}$kg, and the density was $2.76\times10^{3}$ $\mathrm{kg\cdot m^{-3}}$. These measurements enabled calculation of the surface-to-volume ($S/V$) ratio, a key parameter in the subsequent thermal analysis.

### 6.2. Measurement of thermal transport properties

In cylindrical lithium-ion cells, the jelly-roll structure leads to pronounced anisotropy in thermal transport: the electrode–separator stack acts as a parallel configuration in the radial direction and a series configuration in the axial direction. Consequently, radial thermal conductivity ($k_r$) is typically orders of magnitude lower than axial conductivity ($k_z$).

Anisotropic thermal conductivities were measured using a custom-built apparatus equipped with embedded thermocouples and an Agilent 34970A data acquisition system (Figure 6 (b)).

View Article Online
DOI: 10.1039/D5TA09005A

Specific heat capacity ($c_p$) was measured using a calibrated heat capacity analyzer (Thermal Hazard Technology) (Figure 6 (c)). Both measurements were obtained within a single experimental sequence (Figure S2). Heat transfer in the radial direction was modeled as one-dimensional conduction across the cylindrical wall, yielding: $k_r = 0.178 \pm 0.011$ W·m$^{-1}$·K$^{-1}$, $k_z = 18.12 \pm 1.15$ W·m$^{-1}$·K$^{-1}$. These results quantify the intrinsic anisotropy and thermal storage capacity essential for accurate modeling of cell heat transfer.

### 6.3. Accelerating rate calorimetry (ARC) testing

Thermal runaway behavior was evaluated using ARC under near-adiabatic conditions (Figure 6 (d)). During testing, the cell was subjected to incremental heating steps followed by isothermal hold periods until equilibrium was achieved. Once the self-heating rate exceeded a threshold of 0.02 °C·min$^{-1}$, the ARC automatically transitioned to adiabatic tracking, allowing real-time recording of temperature and pressure evolution. This procedure captured temperature-dependent self-heating rates, onset temperature, and maximum temperature rise, enabling the determination of intrinsic reactivity and heat generation rate $Q_{gen}(T)$. These results were later implemented as source terms in the numerical model for predictive simulation of thermal behavior.

### 6.4. Experimental validation of the thermal safety boundary

To validate the simulation-derived thermal safety boundary, a convection-controlled experiment was conducted using a custom apparatus (Figure 6 (e)). The cell was mounted on a heating rack with heating wires to elevate the cell temperature and trigger self-heating. It should be noted that as the temperature raises, the exponential increase in internal chemical reaction heat generation becomes the dominant heat source, far exceeding the external heating input during the

View Article Online
DOI: 10.1039/D5TA09005A

critical transition to thermal runaway. A Nidec fan supplied regulated air flow with a minimum velocity of 0.1 $m\cdot s^{-1}$. Temperature evolution was monitored using the same Agilent data acquisition system.

In each trial, external heating was terminated once the target temperature was reached, allowing the system to evolve under the competing effects of self-heating and convective cooling. The threshold temperature between stabilization and runaway was identified by progressively increasing the setpoint across successive tests. The maximum temperature attained in the last stable trial was recorded as the experimentally validated thermal safety temperature (Figures S10 and S11).

### 6.5. Numerical modeling framework

A physics-based thermal model was developed to simulate heat transfer and predict the critical temperature for runaway initiation (Figure 6 (f)). The model represents the 18650 cell as a homogeneous cylinder with effective anisotropic properties. The transient heat transfer is governed by the energy conservation equation in cylindrical coordinates:

$$\rho c_p \frac{\partial T}{\partial t} = \frac{1}{r}\frac{\partial}{\partial r}\left(k_r r \frac{\partial T}{\partial r}\right) + \frac{\partial}{\partial z}\left(k_z \frac{\partial T}{\partial z}\right) + Q_{gen}(T) \tag{7}$$

The boundary conditions are defined as follows. A convective heat transfer boundary condition is applied to the surfaces of the cell based on Newton's law of cooling:

$$-k\frac{\partial T}{\partial n} = h(T_w - T_{amb}) \tag{8}$$

The simulation is initialized with a uniform temperature field:

$$T(r,z,t=0) = T_0 \tag{9}$$

The jellyroll was discretized into four layers, and temperature-dependent internal heat

View Article Online
DOI: 10.1039/D5TA09005A

generation was implemented via interfacial heat source terms derived directly from the ARC data $Q_{\mathrm{gen}}(T)$. The total heat release was spatially distributed to reflect volumetric reaction behavior while maintaining numerical stability. Heat conduction within the solid domain was coupled with convective boundary conditions on the cell surface, while the bottom face was treated as adiabatic. The initial temperature was prescribed uniformly.

Grid and time-step independence were verified. The model outputs, *i.e.*, including peak temperature, temperature gradients, and critical temperature thresholds, served as the foundation for constructing the thermal safety boundary and calibrating the dimensionless thermal safety criterion.

(a) Mass and volume (b) Thermal conductivity (c) Specific heat (d) ARC testing

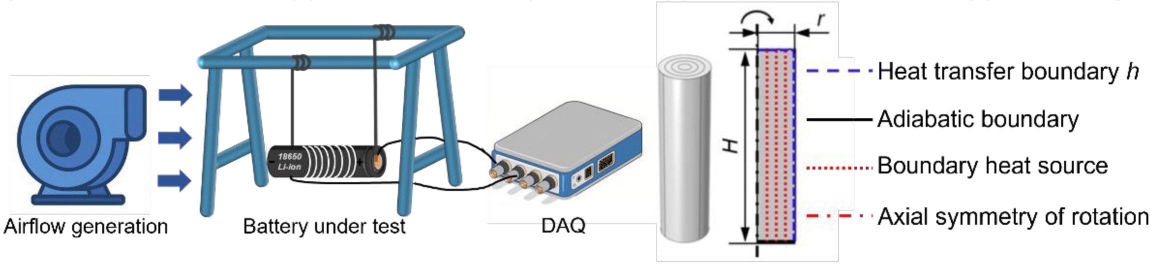

(e) Experimental validation (f) Numerical model

**Figure 6.** Experimental and numerical methodologies.
(a) Physical characterization of the 18650 cell, including mass and volume measurements.
(b) Thermal conductivity measurement setup, with temperature data recorded via thermocouples and processed using an Agilent 34970A data acquisition system.
(c) Specific heat capacity measurement conducted using a Thermal Hazard Technology heat capacity analyzer.
(d) Thermal runaway characterization performed using an accelerating rate calorimeter (ARC) to capture self-heating behavior.
(e) Experimental validation of the thermal safety boundary using a custom-built setup, where the cell was subjected to controlled convection with an adjustable fan speed.

View Article Online
DOI: 10.1039/D5TA09005A

(f) Numerical modeling framework employed to simulate heat transfer and thermal behavior, incorporating experimentally derived heat generation data and convective boundary conditions.

## Data availability

All data underlying the results reported in this study are fully presented within the manuscript.

## Credit author statement

**Jiale Huang:** Methodology, simulation, data analysis, and writing – original draft; **Yiyang Xia:** Experiment and data analysis; **Shijia Xu:** Methodology and writing – review & editing; **Ling Li:** Methodology and writing – review & editing; **Hongbo Ji:** Experiment; **Xiaoping Chen:** Conceptualization and methodology; **Jun Xu:** Conceptualization, methodology, supervision, and writing – review & editing.

## Conflict of Interest

The authors declare that they have no known competing financial interests or personal relationships that could have appeared to influence the work reported in this paper.

## Acknowledgments

XC was supported by National Natural Science Foundation of China (52575509).

## References

[1] Z. Rao, P. Lyu, M. Li, X. Liu, X. Feng, A thermal perspective on battery safety, Nat. Rev. Clean Technol. 1 (2025) 511-524. https://doi.org/10.1038/s44359-025-00073-x

[2] B. Liu, Y. Jia, C. Yuan, L. Wang, X. Gao, S. Yin, J. Xu, Safety issues and mechanisms of lithium-ion battery cell upon mechanical abusive loading: A review, Energy Storage Mater. 24 (2020) 85-112. https://doi.org/10.1016/j.ensm.2019.06.036

[3] X. Gao, C. Chak, Q. Hao, D. Zeng, J. Xu, Thermal safety of lithium-ion batteries: Mechanism, modeling, and characterizations, Annual Rev. Heat Transfer 26 (2023) 69-129. https://doi.org/10.1615/AnnualRevHeatTransfer.2023048695

[4] S. Sun, J. Xu, Safety behaviors and degradation mechanisms of aged batteries: A review, Energy Mater. Devices 2 (2024) 9370048. https://doi.org/10.26599/EMD.2024.9370048

[5] Y. Liu, Y. Tian, Z. Fu, H. Du, B. Li, F. Kang, K. Amine, G. Chen, Thermite reaction-induced

View Article Online
DOI: 10.1039/D5TA09005A

thermal runaway of lithium-ion batteries, Adv. Mater. (2025) e10486. https://doi.org/10.1002/adma.202510486

[6] Z. Cui, A. Manthiram, Thermal stability and outgassing behaviors of high-nickel cathodes in lithium-ion batteries, Angew. Chem. Int. Edit. 62 (2023) e202307243. https://doi.org/10.1002/anie.202307243

[7] L. Huang, G. Xu, X. Du, J. Li, B. Xie, H. Liu, P. Han, S. Dong, G. Cui, L. Chen, Uncovering LiH triggered thermal runaway mechanism of a high-energy $LiNi_{0.5}Co_{0.2}Mn_{0.3}O_2$/graphite pouch cell, Adv. Sci. 8 (2021) 2100676. https://doi.org/10.1002/advs.202100676

[8] Z. Zhong, L. Chen, C. Zhu, W. Ren, L. Kong, Y. Wan, Nano $LiFePO_4$ coated Ni rich composite as cathode for lithium ion batteries with high thermal ability and excellent cycling performance, J. Power Sources 464 (2020) 228235. https://doi.org/10.1016/j.jpowsour.2020.228235

[9] K. Chen, D. Zhang, J. Guo, F. Jiang, N. Shen, X. Yan, W. Zhang, N. Zhu, L. Chen, Y. Zhou, Z. Lyu, G. Xiao, X. Shen, X. Cheng, Y. Wu, Hydrogen generated from binders: An overlooked thermal runaway source in lithium-ion batteries, J. Energy Chem. 109 (2025) 602-608. https://doi.org/10.1016/j.jechem.2025.06.004

[10] H. Zhao, Y. Bai, H. Jin, J. Zhou, X. Wang, C. Wu, Unveiling thermal decomposition kinetics of single-crystalline Ni-rich $LiNi_{0.88}Co_{0.07}Mn_{0.05}O_2$ cathode for safe lithium-ion batteries, Chem. Eng. J. 435 (2022) 134927. https://doi.org/10.1016/j.cej.2022.134927

[11] Y. Wu, X. Liu, L. Wang, X. Feng, D. Ren, Y. Li, X. Rui, Y. Wang, X. Han, G. Xu, H. Wang, L. Lu, X. He, K. Amine, M. Ouyang, Development of cathode-electrolyte-interphase for safer lithium batteries, Energy Storage Mater. 37 (2021) 77-86. https://doi.org/10.1016/j.ensm.2021.02.001

[12] Y. Li, X. Feng, D. Ren, M. Ouyang, L. Lu, X. Han, Thermal runaway triggered by plated lithium on the anode after fast charging, ACS Appl. Mater. Interfaces 11 (2019) 46839-46850. https://doi.org/10.1021/acsami.9b16589

[13] Z. Liu, Y. Jiang, Q. Hu, S. Guo, L. Yu, Q. Li, Q. Liu, X. Hu, Safer lithium-ion batteries from the separator aspect: Development and future perspectives, Energy Environ. Mater. 4 (2021) 336-362. https://doi.org/10.1002/eem2.12129

[14] W. Zhang, X. Feng, L. Lu, H. Wang, L. Wang, X. He, M. Wei, M. Ouyang, Anode failure hunter with a self-quenched function boosting lithium-ion battery safety, ACS Energy Lett. 10 (2025) 4933-4940. https://doi.org/10.1021/acsenergylett.5c02364

[15] Z. Jiang, C. Liu, L. Huang, S. Zhu, X. Zhang, R. Wu, T. Gong, Y. Wu, L. Guo, P. Han, J. Ma, G. Xu, G. Cui, Interfacial reactions take the lead: Elucidating the dominant role of cathode-electrolyte interactions in triggering thermal runaway of high-nickel lithium-ion batteries, Energy Environ. Sci. 18 (2025) 8232-8243. https://doi.org/10.1039/D5EE01431J

[16] X. Ding, X. Wang, C. Zhu, J. Hu, M. Xu, M. Ma, J. Huang, Research on ignition criterion and combustion behavior of aluminum alloy for lithium battery, Sci Rep-UK 15 (2025) 13734. https://doi.org/10.1038/s41598-025-97209-7

[17] X. Feng, M. Fang, X. He, M. Ouyang, L. Lu, H. Wang, M. Zhang, Thermal runaway features of large format prismatic lithium ion battery using extended volume accelerating rate

View Article Online
DOI: 10.1039/D5TA09005A

calorimetry, J. Power Sources 255 (2014) 294-301. https://doi.org/10.1016/j.jpowsour.2014.01.005

[18] X. Feng, D. Ren, S. Zhang, X. He, L. Wang, M. Ouyang, Influence of aging paths on the thermal runaway features of lithium-ion batteries in accelerating rate calorimetry tests, Int. J. Electrochem. Sc. 14 (2019) 44-58. https://doi.org/10.20964/2019.01.14

[19] Y. Wang, K. Zaghib, A. Guerfi, F. F. C. Bazito, R. M. Torresi, J. R. Dahn, Accelerating rate calorimetry studies of the reactions between ionic liquids and charged lithium ion battery electrode materials, Electrochim. Acta 52 (2007) 6346-6352. https://doi.org/10.1016/j.electacta.2007.04.067

[20] J. Lamb, L. Torres-Castro, J. C. Hewson, R. C. Shurtz, Y. Preger, Investigating the role of energy density in thermal runaway of lithium-ion batteries with accelerating rate calorimetry, J. Electrochem. Soc. 168 (2021) 060516. https://doi.org/10.1149/1945-7111/ac0699

[21] S. Zheng, L. Wang, X. Feng, X. He, Probing the heat sources during thermal runaway process by thermal analysis of different battery chemistries, J. Power Sources 378 (2018) 527-536. https://doi.org/10.1016/j.jpowsour.2017.12.050

[22] A. Kriston, I. Adanouj, V. Ruiz, A. Pfrang, Quantification and simulation of thermal decomposition reactions of Li-ion battery materials by simultaneous thermal analysis coupled with gas analysis, J. Power Sources 435 (2019) 226774. https://doi.org/10.1016/j.jpowsour.2019.226774

[23] K. Nam, S. Bak, E. Hu, X. Yu, Y. Zhou, X. Wang, L. Wu, Y. Zhu, K. Chung, X. Yang, Combing in situ synchrotron X-ray diffraction and absorption techniques with transmission electron microscopy to study the origin of thermal instability in overcharged cathode materials for lithium-ion batteries, Adv. Funct. Mater. 23 (2013) 1047-1063. https://doi.org/10.1002/adfm.201200693

[24] C. Liu, S. Reed, A. Manthiram, Delineating the triphasic side reaction products in high-energy density lithium-ion batteries, Adv. Mater. (2025) e09889. https://doi.org/10.1002/adma.202509889

[25] X. Liu, L. Yin, D. Ren, L. Wang, Y. Ren, W. Xu, S. Lapidus, H. Wang, X. He, Z. Chen, G. Xu, M. Ouyang, K. Amine, In situ observation of thermal driven degradation and safety concerns of lithiated graphite anode, Nat. Commun. 12 (2021) 4235. https://doi.org/10.1038/s41467-021-24404-1

[26] Y. Jia, P. Zhao, D. P. Finegan, J. Xu, Dynamics of intra-cell thermal front propagation in lithium-ion battery safety issues, Adv. Energy Mater. 14 (2024) 2400621. https://doi.org/10.1002/aenm.202400621

[27] C. F. Lopez, J. A. Jeevarajan, P. P. Mukherjee, Experimental analysis of thermal runaway and propagation in lithium-ion battery modules, J. Electrochem. Soc. 162 (2015) A1905. https://doi.org/10.1149/2.0921509jes

[28] C. Jin, Y. Sun, J. Yao, X. Feng, X. Lai, K. Shen, H. Wang, X. Rui, C. Xu, Y. Zheng, L. Lu, W. Wang, M. Ouyang, No thermal runaway propagation optimization design of battery arrangement for cell-to-chassis technology, eTransportation 14 (2022) 100199.

View Article Online
DOI: 10.1039/D5TA09005A

https://doi.org/10.1016/j.etran.2022.100199

[29] H. Chen, J. E. H. Buston, J. Gill, D. Howard, R. C. E. Williams, E. Read, A. Abaza, B. Cooper, J. X. Wen, A simplified mathematical model for heating-induced thermal runaway of lithium-ion batteries, J. Electrochem. Soc. 168 (2021) 010502. https://doi.org/10.1149/1945-7111/abd64c

[30] A. Karmakar, H. Zhou, B. S. Vishnugopi, J. A. Jeevarajan, P. P. Mukherjee, State-of-charge implications of thermal runaway in Li-ion cells and modules, J. Electrochem. Soc. 171 (2024) 01529. https://doi.org/10.1149/1945-7111/ad1ecc

[31] C. Wu, M. Tang, W. Peng, A. Shi, S. Gao, S. Zhang, D. Wang, Study on the impact of temperature-dependent anisotropic thermal conductivity on thermal diffusion in lithium-ion batteries, J. Power Sources 622 (2024) 235333. https://doi.org/10.1016/j.jpowsour.2024.235333

[32] X. Liu, T. Zhang, Q. Gao, Z. Han, H. Huang, Y. Xu, H. Chen, X. Xu, The suppression of thermal propagation using spray cooling with R410A in overheated lithium battery pack, Case Stud. Therm. Eng. 58 (2024) 104339. https://doi.org/10.1016/j.csite.2024.104339

[33] Y. Jia, M. Uddin, Y. Li, J. Xu, Thermal runaway propagation behavior within 18650 lithium-ion battery packs: A modeling study, J. Energy Storage 31 (2020) 101668. https://doi.org/10.1016/j.est.2020.101668

[34] Y. Jia, B. Liu, Z. Hong, S. Yin, D. P. Finegan, J. Xu, Safety issues of defective lithium-ion batteries: identification and risk evaluation, J. Mater. Chem. A, 8 (2020) 12472-12484. https://doi.org/10.1039/D0TA04171H

[35] J. Zhao, Z. Lv, D. Li, X. Feng, Z. Wang, Y. Wu, D. Shi, M. Fowler, A. Burke, Battery engineering safety technologies (BEST): M5 framework of mechanisms, modes, metrics, modeling, and mitigation, eTransportation 22 (2024) 100364. https://doi.org/10.1016/j.etran.2024.100364

[36] J. Schoberl, M. Ank, M. Schreiber, N. Wassiliadis, M. Lienkamp, Thermal runaway propagation in automotive lithium-ion batteries with NMC-811 and LFP cathodes: Safety requirements and impact on system integration, eTransporation 19 (2024) 100305. https://doi.org/10.1016/j.etran.2023.100305

[37] L. Wang, Y. Qiu, W. Yuan, Y. Tian, Z. Zhou, Next-generation battery safety management: Machine learning assisted life-time prediction and performance enhancement, J. Energy Chem. 109 (2025) 726-739. https://doi.org/10.1016/j.jechem.2025.05.065

[38] H. Moayedi, Performance improvement and thermal management of a lithium-ion battery by optimizing tab locations and cell aspect ratio, Int. J. Heat Mass Tran., 214 (2023) 124456. https://doi.org/10.1016/j.ijheatmasstransfer.2023.124456

[39] F. Zhang, X. Feng, C. Xu, F. Jiang, M. Ouyang, Thermal runaway front in failure propagation of long-shape lithium-ion battery, Int. J. Heat Mass Tran. 182 (2022) 121928. https://doi.org/10.1016/j.ijheatmasstransfer.2021.121928

[40] C. Mao, M. L. Wang, K. Gao, H. Jin, W. Y. Cho, H. Leon-Rodriguez, K. Hong, S. Han, J. Jeong, H. W. Kang, Dimensionless analysis and novel configuration for enhanced natural convection cooling in lithium-ion batteries, Case Stud. Therm. Eng. 74 (2025) 106766.

View Article Online
DOI: 10.1039/D5TA09005A

https://doi.org/10.1016/j.csite.2025.106766

[41] D. Lee, J. Lee, J. Kim, S. Cho, C. Kim, Thermal behaviors analysis of 55 Ah large-format lithium-ion pouch cells with different cell aspect ratios, tab locations, and C-rates, Appl. Therm. Eng. 175 (2020) 115422. https://doi.org/10.1016/j.applthermaleng.2020.115422

[42] X. Feng, F. Zhang, J. Feng, C. Jin, H. Wang, C. Xu, M. Ouyang, Propagation dynamics of the thermal runaway front in large-scale lithium-ion batteries: Theoretical and experiment validation, Int. J. Heat Mass Tran. 225 (2024) 125393. https://doi.org/10.1016/j.ijheatmasstransfer.2024.125393

[43] D. Dubey, A. Mishra, S. Ghosh, M. Reddy, R. Pandey, Geometry-influenced cooling performance of lithium-ion battery, Appl. Therm. Eng. 230 Part A (2023) 120723. https://doi.org/10.1016/j.applthermaleng.2023.120723

[44] G. Planinšič, M. Vollmer, The surface-to-volume ratio in thermal physics: From cheese cube physics to animal metabolism, Eur. J. Phys. 29 (2008) 369. https://doi.org/10.1088/0143-0807/29/2/017

[45] X. Yi, G. Qi, X, Liu, C. Depcik, L. Liu, Challenges and strategies toward anode materials with different lithium storage mechanisms for rechargeable lithium batteries, J. Energy Storage 95 (2024) 112480. https://doi.org/10.1016/j.est.2024.112480

[46] Z. Wang, C. Xu, L. Chen, J. Si, W. Li, S. Huang, Y. Jiang, Z. Chen, B. Zhao, In-situ lithiation synthesis of nano-sized lithium sulfide/graphene aerogel with covalent bond interaction for inhibiting the polysulfides shuttle of Li-S batteries, Electrochim. Acta 312 (2019) 282-290. https://doi.org/10.1016/j.electacta.2019.04.169

[47] S. Ko, H. Otsuka, S. Kimura, Y. Takagi, S. Yamaguchi, T. Masuda, A. Yamada, Rapid safety screening realized by accelerating rate calorimetry with lab-scale small batteries, Nat. Energy 10 (2025) 707-714. https://doi.org/10.1038/s41560-025-01751-7

[48] J. Holman, Heat Transfer, McGraw-Hill (2009) 10th ed.

[49] N. Semenoff, Zur theorie des verbrennungsprozesses, Zeitschrift für Physik 48 (1928) 571-582. https://doi.org/10.1007/BF01340021

View Article Online
DOI: 10.1039/D5TA09005A

The data supporting this article have been included as part of the Supplementary Information.